

Scalable MHz-Rate Entanglement Distribution in Low-Latency Quantum Networks Interconnecting Heterogeneous Quantum Processors

Jiapeng Zhao,^{1,*} Yang Xu,² Xiyuan Lu,³ Eneet Kaur,¹ Michael Kilzer,¹ Ramana Kompella,¹ Robert W. Boyd,^{4,2,5} and Reza Nejabati¹

¹*Cisco Quantum Labs, 3232 Nebraska Ave, Santa Monica, CA, 90404, USA*

²*Department of Physics and Astronomy,*

University of Rochester, Rochester, NY, 14627, USA

³*Joint Quantum Institute, University of Maryland/NIST, College Park, MD, 20742 USA*

⁴*The Institute of Optics, University of Rochester, Rochester, NY, 14627, USA*

⁵*Department of Physics, University of Ottawa,
Ottawa, Ontario, K1N 6N5, Canada*

(Dated: April 15, 2025)

Abstract

Practical distributed quantum computing and error correction require high-qubit-rate, high-fidelity, and low-reconfiguration-latency quantum networks between heterogeneous quantum information processors. Unfortunately, in a quantum network with homogeneous quantum processors, the theoretical entanglement distribution rate for a single channel is limited to the 100-kHz level with a millisecond-level reconfiguration latency, which is not sufficient for error-corrected distributed quantum computing. Here, we propose a quantum network architecture by introducing the concept of a reconfigurable quantum interface. In our protocol, through tuning the frequency and temporal mode of the photonic qubits to dense wavelength division multiplexing (DWDM) channels, a 4.5 MHz Bell pair distribution rate, with a potential of more than 40 MHz Bell pair rate, is achieved. Through the use of reconfigurable quantum interfaces and wavelength-selective switches, a nanosecond network reconfiguration latency can be demonstrated with low-loss, low-infidelity and high-dimensional switches. To the best of our knowledge, our architecture is the first practical solution that can accommodate the entanglement distribution between heterogeneous quantum nodes with a rate and latency that satisfy most distributed quantum circuits and error correction requirements. The proposed architecture is compatible with the industry-standard DWDM infrastructure, offering a scalable and cost-effective solution for distributed quantum computing.

I. INTRODUCTION

Quantum computers with millions of qubits are critical for achieving practical fault-tolerant quantum computing. For example, factoring a 2,048 bit number using the Shor algorithm requires 20 million qubits [1]. However, due to the limitations of cryogenic cooling power, laser power, etc, it remains very challenging to scale up the number of qubits inside a single quantum processing unit (QPU) beyond 10^4 to meet such a requirement [2].

Alternatively, connecting multiple monolithic quantum processors in a quantum data center via a quantum interface can, in principle, enable millions of qubits to cooperate for various applications. Such a quantum data center includes multiple monolithic QPUs, switches, and communication links. Although physical shuttling of matter qubits between

* penzhao2@cisco.com

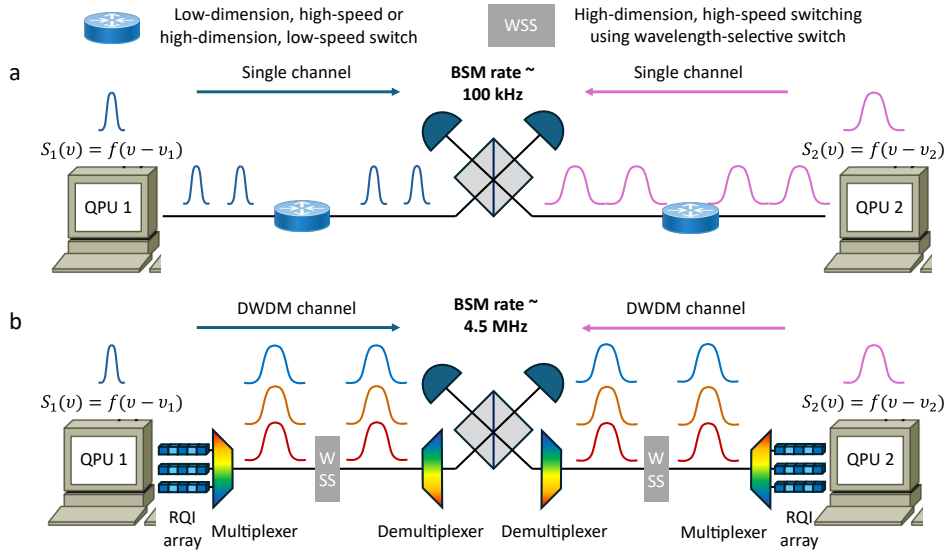


FIG. 1: **a.** The conceptual illustration shows the current quantum network solution for heterogeneous entanglement swapping. The four existing challenges on different components of the quantum network are shown correspondingly. **b.** The conceptual illustration of our scalable, programmable solution for distributing entanglement between heterogeneous quantum information processors, which includes quantum computers, memories and sensors. WSS stands for wavelength-selective switch. The detailed configuration of our system is shown in Fig. 2

QPUs has been demonstrated [3], the photonic quantum interface remains a promising candidate in terms of scaling up to millions of qubits with all-to-all QPU connectivity [4].

The goal of a photonic quantum interface is interconnecting QPUs using an optical fiber networks and enabling high-rate, high-fidelity Bell pair distribution among desired QPUs, which will enable gate and qubit teleportation, as well as error correction in distributed quantum computing [5, 6]. Realizing such a goal relies on the implementation of low-loss, low-noise photonic links with a high information capacity embedded in a reconfigurable, dynamic network, which is very challenging due to the following major obstacles:

1. Most matter qubits cannot be directly entangled with photonic qubits in the low loss telecommunication frequency;
2. The mismatch in the temporal mode of photonic qubits and the transition lineshape

of matter qubits leads to inefficient entanglement swapping;

3. To the best of our knowledge, the upper bound of the entanglement distribution rate of a single channel is limited to the 100 kHz level by the temporal overlap between adjacent single photon wavepackets [7–9].
4. The lack of low-loss, low-crosstalk, high-speed, high-dimensional, high-bandwidth optical switches limits the number of QPUs that can be interconnected within the quantum data center [10–14].

Since the transition frequencies in matter qubits are limited, besides ytterbium, most major matter qubits, including superconducting qubits, trapped ions, cold atoms, color centers and quantum dots, cannot directly entangle with photonic qubits in telecommunication bands [15–26]. However, compared with photons in the telecommunication regime, visible and NIR photons suffer a much stronger loss in standard optical fiber. For example, for a large data center network with a total path length through fiber of 5 km, 780 nm photons from rubidium atoms have about 19 dB more loss than 1550 nm photons. The most widely studied and demonstrated solution to this challenge is through using quantum frequency conversion (QFC) to interface various platforms based on matter qubits to low-loss telecommunication bands [15–45]. This coherent conversion process carries the quantum information from the visible and near-infrared photons to the telecommunication photons, enabling a long-distance entanglement distribution between homogeneous matter qubits.

However, most QFC protocols nowadays focus only on wavelength conversion, and only a few studies discuss the conversion of temporal mode [23, 46, 47]. The optical interaction cross section depends on the temporal mode of the photonic qubits and the lineshape of the matter qubits. In quantum networks with heterogeneous matter qubits, their lineshapes, and hence the temporal mode of emitted photons, usually do not match each other, resulting in a lower entanglement swapping rate. The typical solution is either to use a quantum version of the time lens [23, 46, 47], or to adjust the lineshape of the matter qubits via the Purcell effect. However, in a quantum network with several different matter qubits, reconfiguring the compression ratio in quantum time lens and the Purcell effect to accommodate different species of matter qubits remains challenging and has not yet been demonstrated [48, 49].

Although the successful implementation of QFC has been demonstrated in many experiments, the single-frequency-to-single-frequency conversion protocol has so far failed to allow

multiplexing to achieve a higher Bell pair rate. This fact results in the third challenge: an entanglement distribution rate in a single channel stays at the 100 kHz level. Due to the narrow lineshapes of most transitions in matter qubits, the entangled photonic qubits usually have a broad temporal wavepacket [7–9]. In order to avoid inter-symbol interference between adjacent photonic qubits, the photonic qubit rate for a single channel is thus limited at 100 kHz level [7–9], resulting in a limited Bell swapping rate. This Bell pair distribution rate is not sufficient to execute error-corrected distributed quantum circuits. Executing high-fidelity remote gates in a timely manner requires the MHz rate entanglement distribution, as the two-qubit gate execution time can be sub- μ s level [50–52], and high-fidelity Bell pairs from purification usually consume multiple noisy Bell pairs. Hence, a quantum interface that enables a higher entanglement distribution rate, either through spatial or wavelength multiplexing, is strongly desired, and some early studies indicate possible multiplexing with a limited bandwidth [53].

Unfortunately, the lack of low-loss, low-crosstalk, high-speed, high-dimensional, and large-bandwidth optical switches limits the number of QPUs can be interfaced per network node, further making spatial multiplexing impractical. This challenge comes mainly from the trade-off in optical switches design. Traditional mechanical switches can offer low insertion loss, low crosstalk, large bandwidth, and high dimensional switching at a cost of low speed and large form factor [10–12, 54]. For comparison, photonic switches can offer ps-to-nanosecond level switching with a significantly reduced footprint, enabling a fast execution of distributed quantum circuits. However, loss and crosstalk increase significantly as the dimension (number of ports on the switch) increases [13, 14, 55]. Moreover, photonic switches usually only support a narrow bandwidth of a few nanometers, which is not suitable for the implementation of dense wavelength division multiplexing (DWDM) to boost the entanglement distribution rate. Besides, a slow reconfiguration time of switch can significantly reduce the entanglement distribution rates, introducing non-negligible latency in remote quantum circuit execution [90]. Therefore, a low-loss and low-crosstalk switch with fast reconfiguration speed is still missing for distributed quantum computing (DQC) applications.

Here, we propose a tangible solution, illustrated in Fig. 1(b), to these four challenges based on the concept of reconfigurable quantum interface (RQI). The RQI tunes the frequency and temporal mode of photonic qubits, entangled with matter qubits, to the desired DWDM

channels. Using the mature DWDM infrastructure, our architecture enables an over-MHz rate entanglement distribution with reduced network latency. With realistic experimental parameters, our approach can achieve a Bell pair distribution rate at 4.5 MHz, mainly benefitting from DWDM multiplexing and reduced switching latency. If we adopt the same assumption for the attempt process as in the reference [6], over 40 MHz Bell pair distribution rate can be achieved. The infidelity under tuning is analyzed with a $\chi^{(2)}$ waveguide, and a theoretically noise-free $\chi^{(3)}$ converter is proposed. Meanwhile, by leveraging the wavelength selective switch (WSS) with the integrated RQI array, our architecture can significantly improve the reconfigurability of the network without sacrificing loss, which can satisfy the dynamic entanglement distribution requirement during remote circuit execution.

II. RQI ARCHITECTURE

We use ^{87}Rb atoms as communication qubits in a cold-atom quantum computer to illustrate our RQI architecture and choose parameters following the architecture reported in ref [56]. ^{87}Rb atoms are widely used in quantum computing and quantum sensing [57, 58], and can be conveniently coupled to an optical cavity to enable efficient collection of entangled photons emitted at 780 nm. As shown in Fig. 2(a), we first divide ^{87}Rb atoms into N groups, and the assignment of an atom to a group depends on the circuit execution requirement. Each group of atoms is loaded into an assigned high-collection-efficiency optical microcavity, which corresponds to a DWDM channel. The total number of groups of atoms is the same as the available DWDM channels. The preparation of high-finesse microcavities for quantum processing has been experimentally demonstrated [59–64]. Each group and the corresponding microcavity contain k atoms, where $N_{tot} = kN$ and N_{tot} represent the total number of communication matter qubits available. After the atoms are shuttled into the corresponding cavity, we sequentially excite each atom at each time slot. This process follows the time division multiplexing (TDM) protocol, as shown in Fig. 2(b), proposed by previous literature [7–9, 65, 66].

After the microcavity, the entangled 780 nm photons are collected and then coupled to single mode fibers (SMFs). The SMFs are connected to the corresponding integrated RQI module, which consists of a nonlinear material, tunable lasers, and tuning control. In the first step of conversion, the wavelength of the narrow linewidth, single temporal mode,

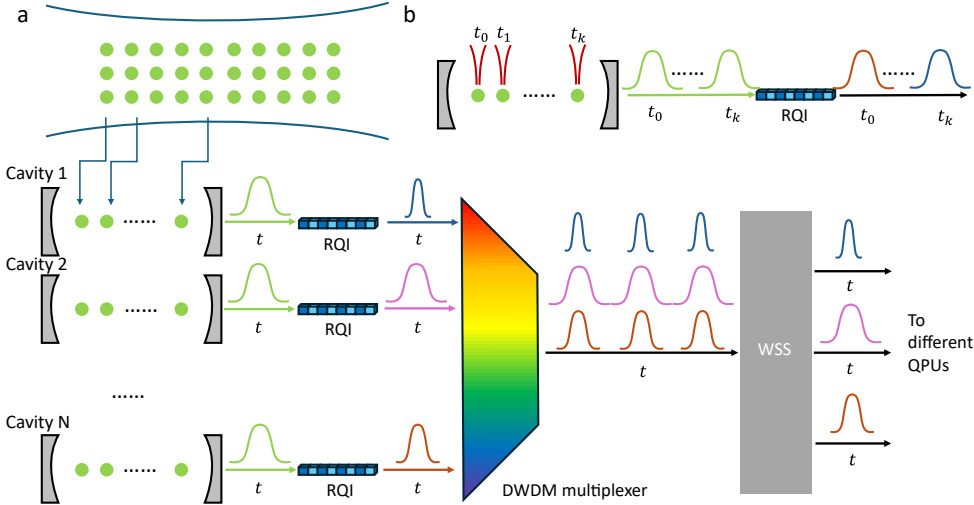


FIG. 2: **a.** The schematic of the RQI system based on ^{87}Rb atoms. Atoms are loaded into microcavities via shuttling. The frequency and temporal mode of entangled photons after each microcavity are programmed to the desired frequency and temporal mode to match the photon used in the Bell swapping procedure. All entangled photons are MUXed via a multiplexer to fully leverage the rate advantage of the standard DWDM protocol. The WSS is used to improve the network reconfigurability which is discussed in more details in Section. V. **b.** The top right figure illustrates the generation of atom-photon entanglement pair using TDM approach. In each microcavity, each atom is prepared and excited sequentially, resulting in the optimal single channel atom-photon entanglement rate. The design and realization of RQI can be found in Section. IV and Fig. 4

mode-hop-free tunable laser is adjusted to the corresponding phase matching wavelength for best frequency conversion efficiency. After the frequency conversion, a pulsed laser with an engineered spectrum is mixed with the entangled photon to convert the temporal mode to the optimal temporal mode. By co-adjusting the tuning parameter, pump laser wavelength, and spectrum, one can convert the entangled photon from 780 nm to arbitrary DWDM channels with the desired temporal mode. It is possible to use a single nonlinear medium with carefully engineered pump pulses that can achieve the single-stage conversion of both frequency and temporal mode. After being multiplexed by a DWDM multiplexer, the converted photons are routed by a WSS to the desired destination, and Bell swapped with another converted photon to achieve remote Bell pair distribution between two QPUs.

The programming of the nonlinear process, either a $\chi^{(2)}$ or $\chi^{(3)}$ process, is usually achieved by tuning the refractive index of the material and the spectrum of the pump laser. The tuning mechanism involves thermal, electrical, optical, and optomechanical tuning with a speed ranging from ns to ms levels, which has been studied and applied to various applications in photonics ranging from visible to microwave bands [67–86]. The on-chip tunable pump laser(s) can be achieved by heterogenous or hybrid integration of the gain medium with tuning realized by photonic integrated circuits [87, 88]. Therefore, reconfiguring the QFC process on integrated photonic circuits is technically available.

III. SIMULATION RESULTS OF ENTANGLEMENT DISTRIBUTION RATES AND FIDELITY

We analyze the performance of our approach under three major scenarios in a quantum data center, including intra-rack, neighboring-rack, and cross-date-center entanglement distribution, using three different configurations, single channel without QFC, single channel with QFC, and RQI DWDM. The simulation results for 9 different combinations are shown in Fig. 3(a), and the details of the pipeline can be found in Appendix B.

These three different scenarios cover different types of distributed quantum computing circuits. For circuits with limited depth, a few tens of QPUs in one single rack is usually adequate to execute the algorithm, and the total intra-rack fiber length is typically a few meters. After circuit partitioning, one single top-of-rack switch is sufficient to route the photonic qubits between different QPUs, but the switch needs to be operated at a high speed, for example μ s time [50–52], to accommodate the 2-qubit gate speed. As shown in the red curves in Fig. 3(a), with or without QFC, the single channel entanglement distribution rate has an upper bound of about 25.2 kHz, which is not fast enough to accommodate the 2-qubit gate speed and satisfy the entanglement distribution rate requirement for error correction. The saturation occurs when the number of communication qubits is above 100. As a comparison, our architecture can offer an entanglement distribution rate of more than 4.5 MHz, and an almost linear dependence between the entanglement distribution rate and the number of communication qubits for $N_{tot} < 1000$. The improvement comes mainly from the DWDM multiplexing and the low-latency switching enabled by our RQI architecture. If we adopt a similar assumption on the entanglement-pair generation rate, the upper bound

of the swap rate for our architecture will be greater than 40 MHz [6]. Therefore, for the execution of small circuits, our architecture ensures that the quantum network will not become the bottleneck.

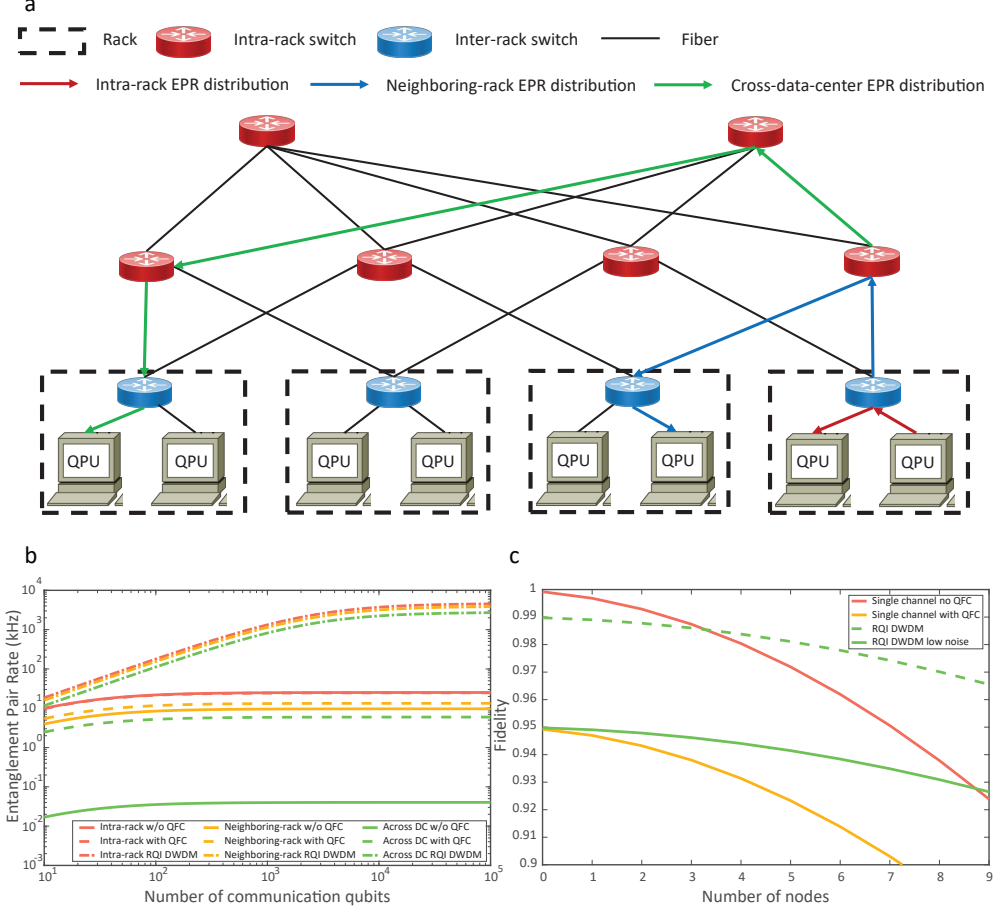


FIG. 3: **a.** An example of quantum data center based on Clos network topology. Three different distributed quantum computing scenarios are illustrated: intra-rack, neighboring-rack, and cross-data-center. **b.** Entanglement distribution rate for single channel without QFC, single channel QFC and DQI DWDM. **c.** Fidelity of distributed photonic qubits as a function of the number of nodes in the network. Entangled photons are assumed to be emitted at optimal rate from each QPU. Details of the simulation pipeline can be found in Appendix B.

When the circuit becomes larger, multiple racks of QPUs are necessary. To reduce the number of switches and the length of the fiber, the distribution of entanglement between neighboring racks becomes the optimal solution, and the length of the fiber is usually tens of

meters. Although careful partitioning of the circuit can reduce the amount of entanglement distribution between racks, it remains challenging to keep all Bell pair distributions within the same rack, as the total number of qubits per QPU is limited [89, 90]. In this scenario, multiple switches are required to provide all-to-all connectivity for QPUs in different racks. As shown in the yellow curves in Fig. 3(a), apparently the single channel solution cannot perform the distributed circuit execution in a timely manner as the entanglement rate is limited to 13.3 kHz with a single channel QFC. If no QFC is implemented, the rate is limited to 9.7 kHz, resulting in a more significant delay in circuit execution. For comparison, our approach still offers up to 3.8 MHz entanglement distribution rate, which is two orders of magnitude faster than the single channel case. The improvement over the single-channel QFC still comes from the DWDM multiplexing and low-loss, low-latency switching, which will be discussed in detail later. Therefore, for medium-size distributed quantum computing jobs, our approach can still satisfy latency requirements.

For circuits requiring millions of qubits, a cross-data center entanglement distribution becomes necessary. In large data centers, the fiber length can be at the level of few km, which introduces significant loss and latency for distributed quantum computing. As a consequence, the single-channel entanglement distribution rate, without any QFC, reduces to 40 Hz as shown in the green curves in Fig. 3(a), becoming the dominant bottleneck for circuit execution. By adopting the single-channel QFC, the rate can be improved to 5.9 kHz, which is still not enough to execute distributed circuit in a timely manner. For comparison, with the RQI DWDM approach, the entanglement distribution rate is capped at 2.7 MHz, which satisfies the execution time of distribution quantum circuits and provides enough photonic qubits for error correction. Therefore, our approach ensures that the execution of distributed quantum jobs will not be delayed by the quantum network.

The fidelity of entangled photons is reduced as a result of network noise, including RQI noise, switch crosstalks, and DWDM multiplexer/demultiplexer noise. We analyze the impact of the network in Fig. 3(b). When the number of nodes through which a photon needs to pass is low, which usually happens in a simple network or during the execution of small circuits, our architecture suffers from greater noise. This is because the RQI we used in this simulation is a noisy $\chi^{(2)}$ converter. When the number of nodes become larger and larger, photons in our architecture suffer less noise than both single-channel with QFC and without QFC. This is mainly because, to keep the reconfiguration rate of the network consistent

with the 2-qubit gate execution time, photonic switches have to be implemented at cost of a higher crosstalk. Compared to mechanical switches, the crosstalk in the photonic switch is usually several orders higher, leading to accumulated infidelity in the network [91]. As we will discuss in the next section, the noise of RQI can be significantly reduced by carefully engineering the nonlinear process, leading to a potential advantage in fidelity even with a small number of nodes, shown in the green dashed line in Fig. 3(b). Thus, our architecture outperforms the conventional approach when the network scales up with higher complexity.

IV. RQI DESIGN

As mentioned above, the noise of our approach comes mainly from RQI noise, DWDM multiplexer/demultiplexer crosstalk, and switch crosstalk. Except for the RQI noise, the rest of the noise can be modeled from the results in literature [10–14, 55, 92–94]. Therefore, our noise and fidelity analysis mainly focuses on the simulation of RQI noise. In this section, we mainly focus on the noise analysis and improvement of the frequency conversion part of the RQI as the relevant research on quantum temporal mode conversion is limited. The diagram of the wavelengths and noise spectrum in our discussion is shown in Fig. 4(a), including the most widely used single stage $\chi^{(2)}$ difference frequency generation (DFG) process, the low-noise $\chi^{(3)}$ converter based on a four-wave mixing Bragg grating (FWM-BG) process, and the theoretical noise-free $\chi^{(3)}$ converter based on third-order difference frequency generation (TDFG) process.

A. RQI based on $\chi^{(2)}$ process

The most widely adopted $\chi^{(2)}$ material for QFC is the periodically poled Lithium Niobate (PPLN) waveguide, which has been demonstrated in single and two-stage conversions [15–22, 24–26, 29, 31–34, 36, 37, 39, 40, 43, 44]. In our ^{87}Rb -780 nm atom-photon entanglement example, thermal tuning of the conversion of the 780 nm photon to DWDM channels, i.e. from 1519.86 nm to 1577.03 nm following ITU standard 50 GHz grid, is analyzed, and the corresponding pump laser wavelength range needs to be from 1543.33 nm to 1602.32 nm.

However, because of the overlap of the frequency band of the converted idler photon with the frequency of the strong pump photon, this conversion is experimentally challenging

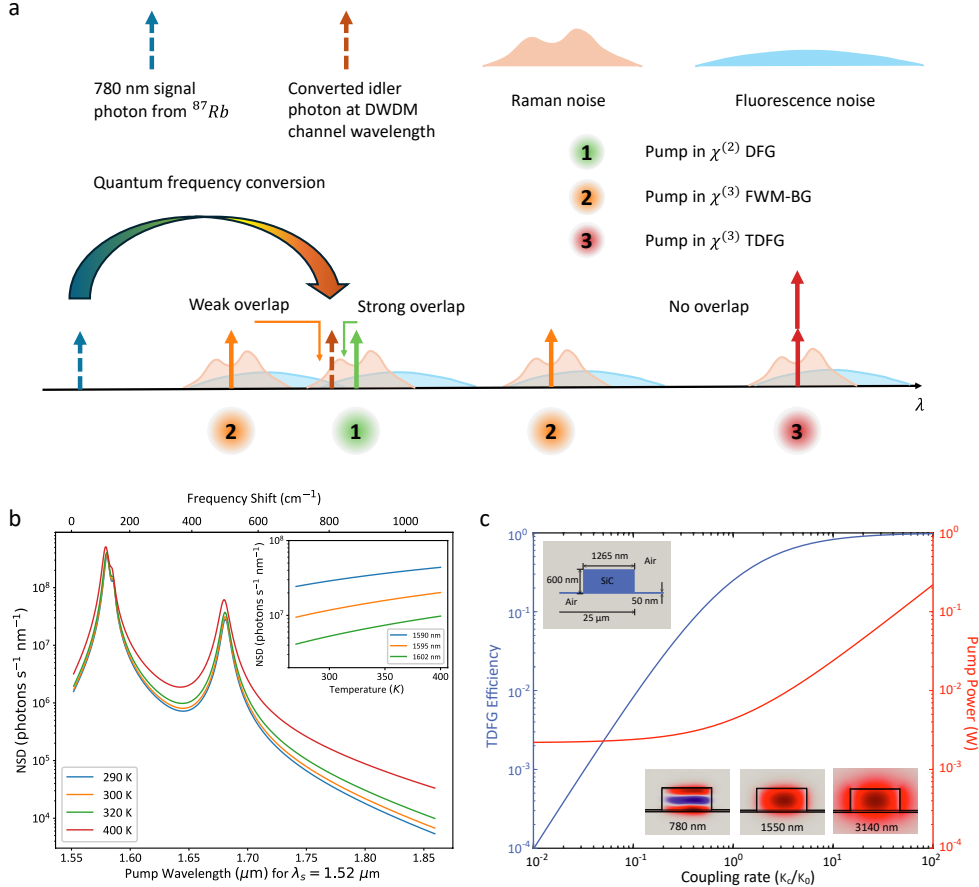


FIG. 4: **a.** Quantum frequency conversion diagram for three nonlinear processes: $\chi^{(2)}$ DFG, $\chi^{(3)}$ FWM-BG, and $\chi^{(3)}$ TDFG. The major noise sources analyzed here are pump-induced Raman noise and fluorescence noise. A spectral overlap between the noise and the dashed arrow indicates that the noise can be found in the conversion. **b.** Noise in a $\chi^{(2)}$ converter as a function of pump wavelength and tuning temperature. **c.** Conversion efficiency and required pump power in a $\chi^{(3)}$ TDFG converter. The device (the top inset) is a silicon carbide microring with a thin bottom support layer with air top and bottom cladding. The optical modes used (the bottom insets) are third-order-vertically transverse-electric mode at 780 nm, and fundamental transverse-electric modes at 1550 nm and 3140 nm.

using the $\chi^{(2)}$ process because of the strong, broadband fluorescence and Raman scattering noise photon from the pump laser. Compared to these two noise sources, noise photons from

photoluminescence and spontaneous-parametric-down-conversion are usually much weaker and thus are ignored here. As shown in Fig. 4, Raman noise has a narrower spectral band than fluorescence noise but is usually stronger with asymmetric Stokes and anti-Stokes spectral noise peaks. The fluorescence noise is usually broader and stronger in the long wavelength regime of the pump, but the peak is generally weaker than the Raman noise. In addition to nonlinear noise, tuning noise, and mode impurity from the pump laser also contribute to the final infidelity of the converted photon. Another reported noise in the PPLN converter comes from the non-uniform poling period during the manufacturing process of the waveguide, which comes from the nanoscale inhomogeneity of the material and can hardly be controlled especially for long waveguides.

Generally speaking, the major noise from PPLN converter can be significantly reduced with a spectrally well-separated pump laser. Therefore, to minimize the noise level, we assume the use of thermal tuning within 20 DWDM channels from 1519.86 nm to 1527.22 nm, and the pump wavelength needs to be tuned from 1594.22 nm to 1602.32 nm. For such a wavelength range, the expected temperature tuning range is 27.26 degree Celsius with 0.27 nm per degree Celsius [31, 95].

Even though the pump photon is about 80 nm away from the idler photon, as shown in Fig. 4(a), the fluorescence noise and Raman noise induced by the pump laser are sufficiently broadband enough to spectrally overlap with the idler photon. Since these spontaneous photons are spectrally indistinguishable from the coherent idler photon, the infidelity is fundamentally nonzero in this single-stage $\chi^{(2)}$ converter. The noise in the PPLN waveguide, designed for the conversion discussed above is shown in Fig. 4(b). Under the strong pumping condition, the internal quantum conversion efficiency can easily reach unit efficiency, but the noise flux is more than 10^6 photons per second per nm at the pump wavelength of interest. Obviously, a longer pump wavelength introduces significantly lower nonlinear noise counts. However, in the $\chi^{(2)}$ process, such a flexibility is not available. Furthermore, the tuning noise can add on top of the nonlinear noise as well, leading to an overall noise above 10^7 photons per second per nm as shown in the sub-figure of Fig. 4b. Without filtering, the noise photon can easily overwhelm the converted idler photon in PPLN converters. Unfortunately, even with strong filtering, as has been demonstrated[15, 16, 43], the noise photon can hardly be reduced to below 50 counts per second, usually leading to an infidelity greater than 5%.

B. RQI based on $\chi^{(3)}$ process

Our example shown in the last section illustrates that, under some circumstances, the fidelity of converted idler photons in the $\chi^{(2)}$ process is fundamentally compromised because of the spectrally indistinguishable spontaneous photons. Although some promising approaches are proposed, for example cascading two PPLN waveguides or cascading multiple narrow-linewidth filters [15, 16, 38, 43], to reduce the noise photon level, significantly higher overall loss is introduced as well, which brings $\chi^{(3)}$ based converter into our consideration.

The $\chi^{(3)}$ process has been investigated for frequency conversion in the past decade, and a possible solution is to choose the spectral location of the two pump laser frequencies in the FWM-BG process to reduce the noise, shown in Fig. 4(a), which has been experimentally demonstrated in both fiber and photonic resonators with over 60% efficiency [30, 35, 41]. According to the nonlinear noise shown in Fig. 4(b), the nonlinear noise from spectrally well-separated pump lasers is significantly lower than the nonlinear noise in the $\chi^{(2)}$ converter. However, the fluorescence noise induced by the pump with a wavelength between that of the signal and idler photon is usually very broad in the long-wavelength regime, and this noise photon can leak into the converted idler photon bandwidth (shown as the leftmost blue noise in Fig. 4(a)). Therefore, this approach still yields, although generally lower than that of the $\chi^{(2)}$ process, some amount of noise, resulting in a limited fidelity.

Alternatively, an advantageous noise-free approach based on third-order difference/sum frequency generation process has also been theoretically proposed [42]. By using two degenerate photons from a mid-IR laser, one can convert the 780 nm photon to the telecommunication band with minimal impact from noise photons generated by high-power lasers, including but not limited to Raman scattering, spontaneous FWM noise, and fluorescence noise. Fig 4(c) shows the simulated photon number efficiency of converting a 780 nm photon to a 1550 nm photon using a pump laser at 3140 nm, and the required pump power assuming the pump laser is critically coupled. To achieve a 90 % conversion efficiency, the microring needs to be 20 times overcoupled at 780 nm and 1550 nm, and the required pump power is only 46 mW. Here we use high-quality 4H-crystalline silicon carbide as the core material [96, 97] with air claddings on top and bottom. This configuration is used not only to confine the optical modes in silicon carbide, but also avoids the noise generation from amorphous materials such as silicon nitride and silicon oxide [98]. While this simulation

result is accurate in concept, we note that the realization of the coupling conditions at these three wavelengths, while maintaining high optical intrinsic qualities, as well as dispersion matching of three modes, requires non-trivial engineering efforts in design and fabrication. Along that end, it is practical to use thermal tuning of the ring resonator to relax the dispersion tolerance. For example, using integrated heaters [99], the dispersion matching of all three wavelengths can be tuned by few tens of nanometers, which is crucial for practical realizations of efficient RQI at targeted wavelengths.

V. IMPROVED NETWORK RECONFIGURABILITY

In addition to the improved entanglement distribution rates, our architecture can significantly improve network reconfigurability, which has been mentioned in recent studies on DWDM-based quantum networking [100–106].

In our architecture, the reconfiguration comes from two aspects by leveraging the wavelength selective switches (WSSs), and the fast reconfiguration speed of RQI. The layout of a WSS is shown in Fig. 5, which consists of DWDM multiplexer/demultiplexer, and one $N \times M$ switch. The first aspect of reconfiguration, which is the main reconfiguration, comes from the $N \times M$ switch inside the WSS, which can offer high-dimension, low-loss, low-crosstalk, and non-blocking all-to-all connectivity using a conventional mechanical switch [11, 12]. The second aspect of reconfiguration, referred as minor reconfiguration, comes from programming the RQI, whose tuning speed can be up to ns [69, 74]. In a minor reconfiguration, the $N \times M$ mechanical switch remains static, but the DWDM channel assigned to each microcavity is changed by reconfiguration of the RQI. This reconfiguration offers limited connectivity but much faster speed, which can satisfy the 2-qubit gate execution time. In a major reconfiguration, both the mechanical switch and DWDM channel assignment are reconfigured, providing arbitrary connectivity, but the rate is limited by the mechanical switch reconfiguration speed, which is usually at the kHz level.

In DQC, one main goal in scheduling is to reduce the distribution of long distance entanglement by carefully partitioning the circuit [89]. In such a scenario, one can ensure that the re-assignment of entanglement between QPUs happens mainly inside each rack, or between neighboring racks [90]. Therefore, during the execution of each job, the reconfiguration of the switch needs to be rapid enough to accommodate 2-qubit gate execution time,

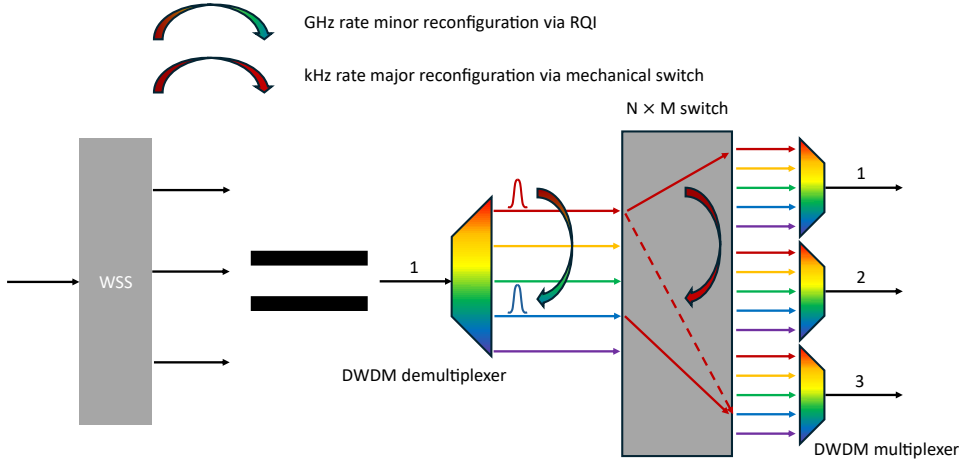


FIG. 5: The illustration of two types of reconfiguration using RQI array and a wavelength selective switch (WSS). Each photon passes through two DWDM multiplexer/demultiplexers and one $N \times M$ switch. The $N \times M$ switch provides all-to-all connectivity, and the M output ports are connected to different DWDM multiplexers. In this example, the $N \times M$ mechanical switch connects ports via solid red lines, and the user needs to reroute the photon from output port 1 to output port 3. If the minor configuration is used, the reconfiguration can be rapidly finished by tuning the photon from the red DWDM channel to blue DWDM channel at GHz level. If the major reconfiguration is used, the $N \times M$ mechanical switch reconfigure the connection from solid red line to dashed red line at kHz rate.

but not dramatic, and most connections in the network are actually not in use. Hence, a minor reconfiguration is usually sufficient during DQC job execution. When loading the new job, based on the partition result, the entire network needs to be reconfigured dramatically, which usually requires a high connectivity in the network, and thus a major reconfiguration is necessary. Since this only happens between DQC jobs, a slow but high-connectivity major reconfiguration does not lead to significant delay. Considering that most useful circuits require lots of distributed Bell pairs, based on our rate simulation shown in Fig. 3(a), the desired major reconfiguration rate of the mechanical switch will be at ms level, which is not challenging for mechanical switches [91].

In our architecture, when a new job is going to be loaded, one first optimizes the partition of the circuit to reduce the number of cross-rack and cross-data center entanglement

distributions. Based on this result, one performs a major reconfiguration of each WSS in the network to best accommodate the ebits distribution for this DQC job. During the job, one only reconfigures the network via programming the RQI at the corresponding QPUs.

Loss plays a significant role in quantum networking. Based on previous experimental results, such a functional WSS can suffer at most 1.5 dB of loss, and a theoretical design has shown the potential to reduce the loss to less than 0.7 dB with a specifically designed DWDM multiplexer/demultiplexer [94]. Compared to the photonic-switch-only approaches, the loss of our approach is significantly lower while the minor reconfiguration speed is at the same level. This result is reached mainly because increasing the dimension of a DWDM multiplexer/demultiplexer does not significantly increase the loss. However, increasing the dimension in a photonic switch usually leads to more loss as the PIC depth goes deeper. Compared to mechanical-switch-only schemes, our approach sacrifices some loss and intra-job network connectivity to gain a significantly faster reconfiguration speed, leading to a much less job execution time for distributed quantum circuits.

VI. DISCUSSION AND CONCLUSION

Although our example is based on cold atoms, the RQI architecture naturally works for other major quantum computing platforms.

Trapped ions constitute a major platform for quantum computing, featuring the highest gate fidelity and all-to-all connectivity. However, scaling up the size of a trapped-ion quantum computer is very challenging, and connecting several QPUs within a quantum network is considered a promising solution. Similarly to neutral atoms, trapped-ion qubits cannot be optically accessed using photons in the telecommunication bands, and thus RQI methods can be used in a useful way [17–22]. The shuttling process in our example can be simplified by assigning each ion chain to an RQI module.

Our architecture is naturally compatible with color-center quantum memories, including SiV, NV, and SnV. One major challenge in the use of color centers comes from the variation in resonance frequencies for different color centers. Although recent demonstrations have shown possible tuning of the resonance, an average of the 2 GHz tuning range can hardly mitigate the resonance mismatch between different color centers [107]. Considering that QFC has been demonstrated to be essential for color centers in quantum networks [23–26],

our approach can solve frequency variations in different color center samples, as well as significantly improve the entanglement rate.

Quantum dots are considered to be a promising candidate for deterministic single-photon emission for many quantum information applications. However, fabricating identical quantum dots remains a challenge, and the wavelength is usually randomly distributed around the desired wavelength because of spectral diffusion. To interfere photons from multiple quantum dots, QFC needs to be implemented. Therefore, with RQI, one can easily multiplex and Bell swap photons emitted by spectrally distinguishable dots without the concern of fabrication defects.

In summary, we propose a quantum networking architecture based on RQI to improve the entanglement distribution rate and reduce the reconfiguration latency. As summarized in Table I, compared to current quantum network architectures, our architecture can improve the entanglement distribution rate to be greater than 4.5 MHz, with a potential of more than 40 MHz, using the industrial standard DWDM protocol. By dropping inessential connectivity within the circuit execution, the reconfiguration time can be reduced down to the nanosecond level without sacrificing the entanglement distribution rate and fidelity. In terms of the RQI design, we analyze the infidelity induced by noisy $\chi^{(2)}$ converters and

TABLE I: A comparison of distributed quantum computing metrics between our RQI architecture and current solutions. Rate represents the entanglement distribution rate.

	Single channel without QFC	Single channel with QFC	RQI DWDM
Intra-rack Rate (kHz) ^a	25.16	24.66	4508
Inter-rack Rate (kHz)	9.66	13.34	3844
Intra-rack Rate (kHz)	0.040	5.96	2696
Fidelity ^b (3 nodes)	0.987	0.938	0.946
Fidelity ^b (9 nodes)	0.924	0.878	0.926
Latency	~ns	~ns	~ns
Connectivity	All-to-all	All-to-all	All-to-all ^c

^a Assume use GHz photonic switch.

^b Assume perfect atom-photon entanglement.

^c All-to-all connectivity in major reconfiguration.

propose a theoretically noise-free $\chi^{(3)}$ converter design. To the best of our knowledge, this is the first architecture to satisfy the entanglement distribution rate requirement for distributed quantum computing and error correction. Our approach is based on the standard DWDM infrastructure, which indicates a promising low-cost solution to enable distributed quantum computing.

ACKNOWLEDGMENTS

The authors acknowledge the helpful discussion from Hassan Shapourian and Galan Moody, as well as the support of PPLN waveguide design and fabrication from Dr. Shijie Liu and Prof. Yuanlin Zheng at Shanghai Jiao Tong University.

COMPETING INTEREST

Jiapeng Zhao, Eneet Kaur, Michael Kilzer, and Reza Nejabati are listed as innovators of the US patent application (serial number: 18/952,548) on the reconfigurable quantum interface.

Appendix A: Intra-cavity TDM

For each atom inside the microcavity, the main time overhead during the generation of atom-photon entanglement pairs comes from the atom shuttling ($\sim 100\mu\text{s}$) and initialization ($\sim 10\mu\text{s}$). To average out this time consumption, a time division multiplexing (TDM) approach was proposed, which can significantly improve the photon-atom entanglement rate [7–9, 65, 66]. Therefore, the first step of our approach follows the TDM approach to maximize the atom-photon entanglement rate of each microcavity. In our architecture, during the loading process, one no longer shuttles the atoms into one single large cavity, but shuttles atoms into each microcavity in parallel and then applies the initialization pulse to atoms in each microcavity.

As mentioned in the main text, we first divide ^{87}Rb atoms into N groups, and then load each group of atoms into microcavities, which correspond to N DWDM channels. Each cavity contains k atoms, where $N_{tot} = kN$ and N_{tot} represent the total number of

communication qubits available. After initializing the k atoms inside each cavity, the atoms are prepared in the ground state $|\psi_g\rangle^{\otimes k} = [(|0_g\rangle + |1_g\rangle)/\sqrt{2}]^{\otimes k}$, which corresponds to the $5S_{1/2}$ state of ^{87}Rb . The detuning of the pump laser pulse needs to be designed to minimize the scattered light from the pumping laser pulse.

During the first round of attempts, N copies of laser pulses excite the first atom inside each microcavity to the excited state $5P_{3/2}$, and then decay to the lower level with the emission of a single photon at 780 nm, leading to an atom-photon entanglement state of $|\psi_{AP}\rangle = 1/\sqrt{2}(|\downarrow\rangle|V\rangle + |\uparrow\rangle|H\rangle)$ [15, 16]. The temporal profile of the excitation laser is engineered to optimize the temporal mode of the emitted photon for the highest possible rates [108]. Although this temporal mode may not be the optimal mode for swapping, the RQI can adjust it after microcavity. The operation is repeated for each atom within the microcavity for k times, and each round of operation usually takes around $1\mu\text{s}$, resulting in a total of $k\mu\text{s}$. During the operation, the successfully entangled atoms are shuttled out. After the M round of attempts, another k atoms will be reloaded and initialized. The number of the round of attempts M should also be optimized to maximize the generation of atom-photon entanglement pairs within each cavity. Based on these parameters, the Bell pair distribution rate R_{bp} can be found as [7, 8]:

$$R_{bp} = \frac{\sum_{i=1}^M N_i P_{suc}}{t_{move} + Mt_{init} + \sum_{i=1}^M N_i t_{ent}}, \quad (\text{A1})$$

where $N_i = N_{i-1}(1 - P_{suc})$ represents the number of entanglement attempts in round i and t_{move} represents the atom shuttling time from the storage zone to the cavity. P_{suc} is the probability of a successful Bell swap in each attempt. The details of finding this probability can be found in Appendix B. t_{init} is the initialization time after the atoms are loaded into the microcavity, and t_{ent} is the time to attempt entanglement generation for each atom in the cavity. To be consistent with previous works, we set $t_{move} = 100\mu\text{s}$, $t_{init} = 10\mu\text{s}$, $t_{ent} = 1.09\mu\text{s}$ and $M = 5$ in our simulations [7, 8]. In the ideal case without loss, an upper bound of the Bell swap rate between two atoms can be found as 229.3 kHz.

Recently, a new research has mentioned that it is possible to have a higher attempt rate and a lower initialization time for atoms [6]. After adopting the new parameters, a higher upper bound of the entanglement rate between two atoms is found to be 2.3 MHz.

Appendix B: Rate and fidelity simulation pipeline

Now we discuss how we calculate P_{suc} in our rate simulation. We assume that the ^{87}Rb atom has a photon emission in cavity probability of 0.5. The collection efficiency for this photon $\eta_{col} = 0.96$ and a SMF coupling efficiency η_{coup} of 0.9, which is consistent with previous work [7, 8, 56]. The typical fiber loss for DWDM channels is $l_{tele} = 0.17\text{dB/km}$ (Corning SMF-28), and for 780 nm, the loss l_{NIR} is usually around 4dB/km (Corning HI780). Another major loss is the insertion loss from switches and DWDM multiplexers/demultiplexers. A designated quantum matrix switch can have a typical insertion loss of 0.35 dB and the worst insertion loss of 0.7 dB for DWDM channels [93], while such a switch in NIR can have a loss of more than 2 dB. A much higher-dimension switch is also available with a similar performance in terms of loss (worst loss less than 1 dB for the 192×192 switch) [109]. Note that, the crosstalk for these mechanical-based optical switches is usually less than 70 dB, which is significantly lower than the photonics counterparts. The switch loss 1.33 dB used by previous work only supports telecommunication bands with mechanical switches [7, 10, 91, 110]. For photonic switches, the state-of-art loss is found to be around 4 dB for a 2 by 8 switch [111]. Considering that the technology for photonic switches is growing rapidly, we use a 2 dB loss for photonic switches for even high-dimensional switches in our simulation.

The state-of-the-art insertion loss of a DWDM multiplexer/demultiplexer is $l_{MUX} = 0.5$ dB [92, 94, 112]. A low-loss grating-based DWDM multiplexer/demultiplexer with insertion loss of 0.137 dB has been demonstrated [94]. The detector efficiency is chosen to be $\eta_D = 0.95$, which has been experimentally demonstrated in Niobium Nitride superconducting nanowire single photon detectors [113]. For RQI, we assume that the conversion has a quantum efficiency η_{QE} of 1, which is the designed efficiency of our PPLN waveguide, and is similar to the previous demonstrated internal efficiency [15, 16]. The fiber-to-chip and chip-to-fiber coupling efficiency η_{chip} has been demonstrated to be 0.97, which is also the coupling efficiency for the photonic switch in our simulation [114, 115]. A spectral filtering efficiency $\eta_{FP} = 0.95$ is selected, which is similar to the Fabry-Perot filter efficiency reported before [16, 25, 43].

In our rate simulation, we assume that the network orchestrator has assigned the optimal wavelength and temporal mode for the RQIs on both QPUs, and the atoms in both micro-cavities behind the RQI are attempted following the TDM discussed before. The circuits

are first partitioned into several QPUs, and we assume each QPU needs 100 distributed Bell pairs before reconfiguring the network. Inside each QPU, we assume that the communication qubits keep emitting entangled photons unless the switch is under reconfiguration. The reconfiguration of RQI can happen during the network reconfiguration and the generation of entangled photons. The configuration speed of the RQI is assumed to be 1 ns, and thus the WSS minor reconfiguration rate is at 1 GHz. The classical communication in the network is ignored at the moment.

In the no-RQI case without QFC, the entangled photons are directly out-coupled into SMF by collection optics, and then routed by NIR switch to the desired BSM module. The NIR switch is assumed to be an integrated photonic switch to satisfy the latency requirement for DQC jobs. A low-loss but slow mechanic switch in the network will result in a long holding time during circuit execution, which also leads to a lower entanglement distribution rate. For simplicity, we assume that the loss of the photonic switch at the NIR bands has a loss similar to the loss of the photonic switch at DWDM bands. Each BSM module uses the standard linear optics BSM configuration, indicating a success rate of 50%. Since the overall efficiency of enhanced BSM is not yet ideal, we would not consider it in our scheme.

In the no-RQI case with QFC, the entangled photons are directly out-coupled into SMF by collection optics. The frequency is converted to a single channel in the DWDM band. The switch is assumed to be an integrated photonic switch at DWDM channels to satisfy the latency requirement for DQC jobs. The rest is the same as the previous case.

In the RQI case with DWDM, the photons are firstly coupled in the RQI module with a efficiency as mentioned before. After the nonlinear media, photons are coupled into a DWDM multiplexer, and then sent to a WSS for routing. The RQI in our case is assumed to be reconfigured at 1 ns, which adds negligible latency to the network and thus leads to almost no reduction in entanglement distribution rates. Photons pass through two DWDM multiplexer/demultiplexer and one mechanical switch, whose losses have been mentioned above. We assume that all DWDM channels are available for distributing Bell pairs and the essential classical communications are in a different fiber or channel, for example, telecommunication O band.

In the fidelity simulation, each node consists of one switch or WSS. For RQI with DWDM, each photon travel through one RQI, one DWDM multiplexer and N nodes to be Bell swapped. In the no-RQI but-with-QFC case, only the infidelity from the QFC and switch

are considered. The infidelity of each photonic switch is assumed to be 25 dB, and the infidelity of each mechanical switch is assumed to be 60 dB.

Appendix C: Raman noise analysis in PPLN waveguides

The spontaneous Raman scattering (SRS) is a nonlinear optical process where a pump photon scatters off a phonon in a material creating a redshifted (Stokes) photon by exciting a phonon mode or a blueshifted (anti-Stokes) photon by absorbing the phonon. SRS has been shown to generate Raman-shifted photons over a broad spectral range, and thus is considered a major noise source in common $\chi^{(2)}$ QFC devices such as PPLN waveguides. When the QFC waveguide is pumped by an intense narrowband laser source, the spectrum of the generated broadband Raman photons usually includes a small but non-negligible frequency component that equals the frequency of the parametrically converted photons, lowering the fidelity of the converted quantum state. Hence, a full characterization of the SRS noise is necessary for the optimal design of $\chi^{(2)}$ QFC devices.

PPLN waveguide has been established as a widely-adopted QFC device based on its $\chi^{(2)}$ nonlinearity because of its low loss and excellent temperature tunability. The Raman scattering in LiNbO_3 (LN) was thoroughly studied in early studies by Loudon [116], Johnston and Kaminow [117]. It was found that the spectral response of Raman scattering is best described by a sum of Lorentzian distributions since the phonon modes in materials are generally well fitted by Lorentzians. Therefore, the Raman response of lithium niobate, also known as the Raman susceptibility, can be written as

$$\chi_R(\Omega) = \sum_{j=1}^N \frac{f_j}{\omega_j^2 + 2i\gamma_j\Omega - \Omega^2} \quad (\text{C1})$$

where N is the total number of optical phonon modes. $\Omega = \omega_s - \omega_0$ is the difference between the scattered photon frequency ω_s and the pump frequency ω_0 . ω_j , γ_j and f_j are the peak frequency, the line width and the weight parameter to be fitted for the j -th phonon mode. For our PPLN waveguide (5% MgO:LN), we use the table of fit parameters in [118]. A detailed classical treatment using the Raman susceptibility χ_R has been presented in [119]. In our PPLN ridge waveguide for QFC purposes, we only consider one spatial mode supported by the waveguide at a specific frequency, and we apply a quantum mechanical model [120] to describe the noise spectrum of Raman photons. To find the Raman noise spectrum, we can

write the following Raman photon-number evolution equation the from the coupled wave equations [120]

$$\frac{dN_s}{dz} = \frac{3\omega_s}{2n_s n_0 \epsilon_0 c^2} \text{Im}[\chi_R(\Omega)] h(\Omega) \Theta_R(N_s + 1) \quad (\text{C2})$$

where N_s is the number of Raman scattered photons, $\text{Im}[\chi_R(\Omega)]$ is the imaginary part of the Raman susceptibility, P_0 is the pump power and n_s , n_0 are the refractive indices of the scattered light and the pump respectively. Θ_R is the modal overlap integral of the Raman scattering process

$$\Theta_R = \iint |u_0(x, y)|^2 |u_s(x, y)|^2 dx dy \quad (\text{C3})$$

where $u_0(x, y)$ and $u_s(x, y)$ are the spatial profile of the pump and the Raman scattered photons inside the waveguide. Note that the Raman noise also depends on the average phonon number $h(\Omega)$ which can be determined by summing across all vibrational energy levels of the phonon modes of the system. For Stokes and anti-Stokes Raman scattering, $h(\Omega)$ takes the following form

$$h(\Omega < 0) = 1 + \langle n(|\Omega|) \rangle \quad (\text{C4a})$$

$$h(\Omega > 0) = \langle n(|\Omega|) \rangle \quad (\text{C4b})$$

$\langle n(|\Omega|) \rangle$ is the average phonon number of the system and follows the Boltzmann distribution

$$\langle n(|\Omega|) \rangle = \frac{1}{e^{\hbar|\Omega|/k_B T} - 1} \quad (\text{C5})$$

where T is the temperature of the system. Solving Eq. C2 for a propagation length $z = L$ in the device, we get the Raman noise spectral density (NSD)

$$\frac{dN_s}{d\lambda} = \frac{6\pi^2 P_0 h(\Omega) \Theta_R \text{Im}[\chi_R(\Omega)] L}{\epsilon_0 \lambda_s^3 n_s n_0}. \quad (\text{C6})$$

In our tunable QFC device, we meet the phase-matching condition for a broad range of wavelengths by tuning the temperature of our PPLN waveguide. Therefore, the change in the noise spectrum in Eq. C6 due to the temperature change should be estimated for the optimal design. A change in temperature not only affects the average phonon number in a specific mode, $h(\Omega)$ but also shifts the peak position and the line width of the Raman susceptibility of the material [121]. For the x-cut LN at room temperature, only three A_1

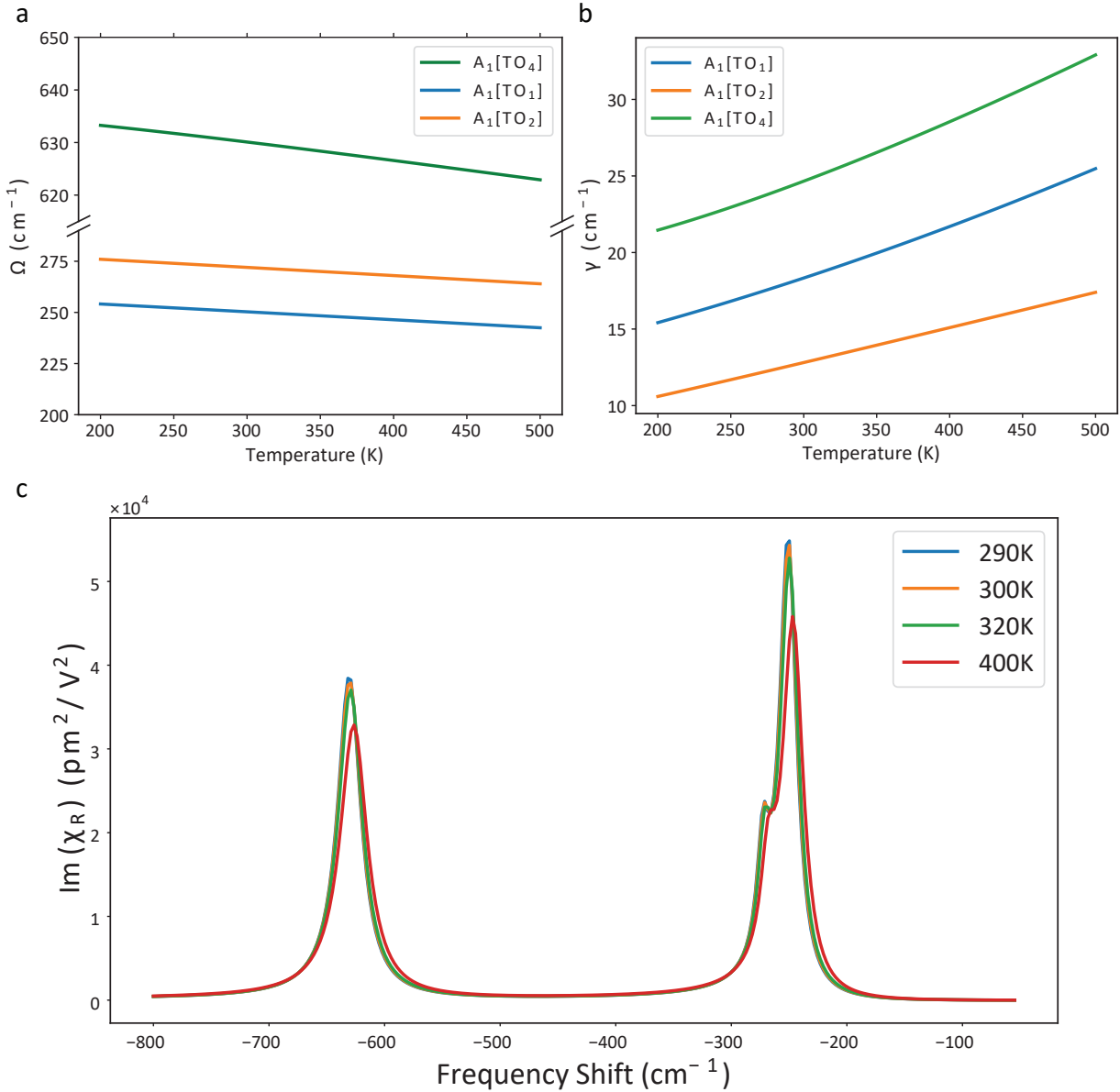


FIG. 6: **a.** Temperature-dependent peak frequency shift of the three dominant optical phonon modes ($A_1[TO_1]$, $A_1[TO_2]$ and $A_1[TO_4]$) in an x-cut 5% MgO: LN crystal. Note that the resonance frequency of the phonon modes experiences a redshift as the temperature of the crystal increases. **b.** Temperature-dependent line width change of the three dominant optical phonon modes ($A_1[TO_1]$, $A_1[TO_2]$ and $A_1[TO_4]$) in an x-cut 5% MgO: LN crystal. Note that the line width of the Lorentzian increases as the temperature of the crystal rises. **c.** The imaginary part of the Raman susceptibility $Im[\chi_R]$ of the x-cut 5% MgO:LN crystal under different temperature. The Raman susceptibilities differ at different temperatures mainly because of the shift of the peak frequencies and the line broadening shown in **a** and **b**.

phonon modes peaked at 252 cm^{-1} ($\text{A}_1[\text{TO}_1]$), 274 cm^{-1} ($\text{A}_1[\text{TO}_2]$) and 632 cm^{-1} ($\text{A}_1[\text{TO}_4]$) have dominant contributions to the Raman susceptibility. We use the model presented in [122] to describe the temperature dependence of the peak and line width change due to the anharmonic properties in LN. The temperature dependence of each optical phonon frequency $\omega(T)$ and phonon damping $\gamma(T)$ are given by

$$\omega(T) = \omega(0)(1 + KT) - D \left[1 + 2n \left(\frac{\omega(0)}{2} \right) \right] \quad (\text{C7a})$$

$$\gamma(T) = \gamma(0) + B \left[1 + 2n \left(\frac{\omega(0)}{2} \right) \right] + CT^2 \quad (\text{C7b})$$

where $n(\omega) = \frac{1}{e^{\hbar\omega/k_B T} - 1}$. $B, C, D, K, \omega(0)$ and $\gamma(0)$ are fitting parameters whose values are presented in Table 1 of [122].

Fig. 6(a) and 6(b) show the temperature-dependent peak frequency and the line width of the three dominant optical phonon modes in an x-cut 5% MgO:LN crystal. The peak frequency undergoes a slight redshift, and the line width increases as the temperature of the system rises. Such temperature-dependent variation gives rise to a noticeable change in the Raman susceptibility curve whose imaginary part is shown in Fig. 6(c).

Considering the temperature dependence of the Raman susceptibility, we can now determine the noise spectrum density $\frac{dN_s}{d\lambda}$ as a function of the Raman shift Ω for a pump power $P_0 = 200\text{ mW}$ and a waveguide length of 3 cm. The anti-Stokes scattering is much weaker than the Stokes scattering because of the difference in the Bose-Einstein population factor, so a long-wavelength pump scheme (the wavelength of the pump is the largest among all three waves being mixed) is usually adopted in common QFC devices. Therefore, only anti-Stokes scattering is considered as the main source of Raman noise in the main text. The curves in Fig. 7 in the Appendix show the noise spectral density of the Stokes photons under different temperatures for a target signal wavelength at $1.52\text{ }\mu\text{m}$. As the pump wavelength moves further away from the target signal wavelength, the Stokes scattering is dramatically suppressed. However, compared to the anti-Stokes scattering shown in Fig. 4(b) of the main text, the Stokes scattering noise is, on average, one to two orders of magnitude higher than the anti-Stokes noise, and the anti-Stokes component becomes more sensitive to the temperature change at longer pump wavelengths. Hence, the difference frequency generation with a long-wavelength pump is well justified in our QFC application.

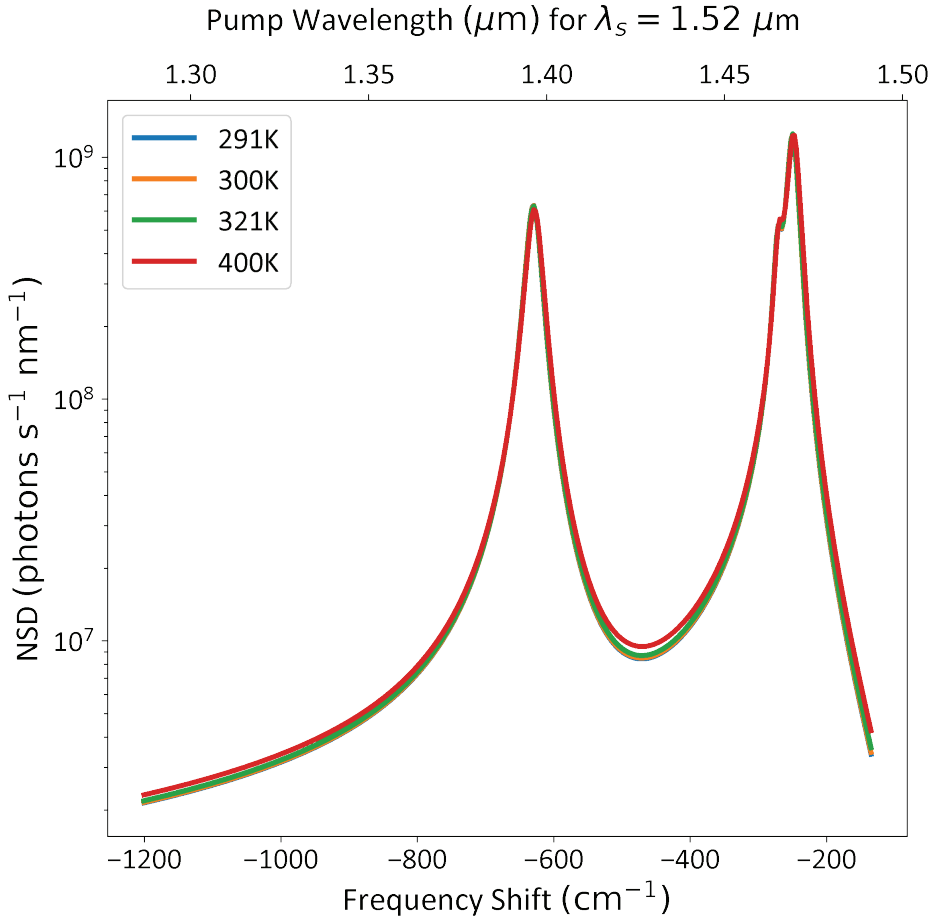


FIG. 7: Noise in a $\chi^{(2)}$ converter due to Stokes scattering as a function of pump wavelength and tuning temperature. The Stokes scattering is stronger than the anti-Stokes scattering noise by two orders of magnitude.

[1] C. Gidney and M. Ekerå, How to factor 2048 bit rsa integers in 8 hours using 20 million noisy qubits, *Quantum* **5**, 433 (2021).

[2] H. J. Manetsch, G. Nomura, E. Bataille, K. H. Leung, X. Lv, and M. Endres, A tweezer array with 6100 highly coherent atomic qubits, arXiv preprint arXiv:2403.12021 (2024).

[3] M. Akhtar, F. Bonus, F. Lebrun-Gallagher, N. Johnson, M. Siegele-Brown, S. Hong, S. Hile, S. Kulmiya, S. Weidt, and W. Hensinger, A high-fidelity quantum matter-link between ion-trap microchip modules, *Nature communications* **14**, 531 (2023).

- [4] D. Main, P. Drmota, D. Nadlinger, E. Ainley, A. Agrawal, B. Nichol, R. Srinivas, G. Araneda, and D. Lucas, Distributed quantum computing across an optical network link, *Nature* , 1 (2025).
- [5] J. Ramette, J. Sinclair, N. P. Breuckmann, and V. Vuletić, Fault-tolerant connection of error-corrected qubits with noisy links, *npj Quantum Information* **10**, 58 (2024).
- [6] J. Sinclair, J. Ramette, B. Grinkemeyer, D. Bluvstein, M. Lukin, and V. Vuletić, Fault-tolerant optical interconnects for neutral-atom arrays, *arXiv preprint arXiv:2408.08955* (2024).
- [7] Y. Li and J. D. Thompson, High-rate and high-fidelity modular interconnects between neutral atom quantum processors, *PRX Quantum* **5**, 020363 (2024).
- [8] S. Sunami, S. Tamiya, R. Inoue, H. Yamasaki, and A. Goban, Scalable networking of neutral-atom qubits: Nanofiber-based approach for multiprocessor fault-tolerant quantum computer, *arXiv preprint arXiv:2407.11111* (2024).
- [9] L. Hartung, M. Seubert, S. Welte, E. Distante, and G. Rempe, A quantum-network register assembled with optical tweezers in an optical cavity, *Science* **385**, 179 (2024).
- [10] W. M. Mellette and J. E. Ford, Scaling limits of mems beam-steering switches for data center networks, *Journal of Lightwave Technology* **33**, 3308 (2015).
- [11] A. S. Khope, M. Saeidi, R. Yu, X. Wu, A. M. Netherton, Y. Liu, Z. Zhang, Y. Xia, G. Fleeman, A. Spott, *et al.*, Multi-wavelength selective crossbar switch, *Optics express* **27**, 5203 (2019).
- [12] Y. Ma, L. Stewart, J. Armstrong, I. G. Clarke, and G. Baxter, Recent progress of wavelength selective switch, *Journal of Lightwave Technology* **39**, 896 (2020).
- [13] X. Sun, J. Feng, L. Zhong, H. Lu, W. Han, F. Zhang, R. Akimoto, and H. Zeng, Silicon nitride based polarization-independent 4×4 optical matrix switch, *Optics & Laser Technology* **119**, 105641 (2019).
- [14] S. Bartolucci, P. Birchall, D. Bonneau, H. Cable, M. Gimeno-Segovia, K. Kieling, N. Nickerson, T. Rudolph, and C. Sparrow, Switch networks for photonic fusion-based quantum computing, *arXiv preprint arXiv:2109.13760* (2021).
- [15] T. van Leent, M. Bock, R. Garthoff, K. Redeker, W. Zhang, T. Bauer, W. Rosenfeld, C. Becher, and H. Weinfurter, Long-distance distribution of atom-photon entanglement at telecom wavelength, *Physical Review Letters* **124**, 010510 (2020).

- [16] Y. Zhou, P. Malik, F. Fertig, M. Bock, T. Bauer, T. van Leent, W. Zhang, C. Becher, and H. Weinfurter, Long-lived quantum memory enabling atom-photon entanglement over 101 km of telecom fiber, *PRX Quantum* **5**, 020307 (2024).
- [17] J. D. Siverns, X. Li, and Q. Quraishi, Ion–photon entanglement and quantum frequency conversion with trapped Ba^+ ions, *Applied optics* **56**, B222 (2017).
- [18] M. Bock, P. Eich, S. Kucera, M. Kreis, A. Lenhard, C. Becher, and J. Eschner, High-fidelity entanglement between a trapped ion and a telecom photon via quantum frequency conversion, *Nature communications* **9**, 1998 (2018).
- [19] V. Krutyanskiy, M. Meraner, J. Schupp, V. Krcmarsky, H. Hainzer, and B. P. Lanyon, Light-matter entanglement over 50 km of optical fibre, *npj Quantum Information* **5**, 72 (2019).
- [20] J. Hannegan, U. Saha, J. D. Siverns, J. Cassell, E. Waks, and Q. Quraishi, C-band single photons from a trapped ion via two-stage frequency conversion, *Applied Physics Letters* **119** (2021).
- [21] U. Saha, J. D. Siverns, J. Hannegan, Q. Quraishi, and E. Waks, Low-noise quantum frequency conversion of photons from a trapped barium ion to the telecom o-band, *ACS Photonics* **10**, 2861 (2023).
- [22] V. Krutyanskiy, M. Canteri, M. Meraner, V. Krcmarsky, and B. Lanyon, Multimode ion-photon entanglement over 101 kilometers, *PRX Quantum* **5**, 020308 (2024).
- [23] K. A. Fisher, D. G. England, J.-P. W. MacLean, P. J. Bustard, K. J. Resch, and B. J. Sussman, Frequency and bandwidth conversion of single photons in a room-temperature diamond quantum memory, *Nature communications* **7**, 11200 (2016).
- [24] A. Stolk, K. L. van der Enden, M.-C. Roehsner, A. Teepe, S. O. Faes, C. Bradley, S. Cadot, J. van Rantwijk, I. Te Raa, R. Hagen, *et al.*, Telecom-band quantum interference of frequency-converted photons from remote detuned nv centers, *PRX Quantum* **3**, 020359 (2022).
- [25] E. Bersin, M. Sutula, Y. Q. Huan, A. Suleymanzade, D. R. Assumpcao, Y.-C. Wei, P.-J. Stas, C. M. Knaut, E. N. Knall, C. Langrock, *et al.*, Telecom networking with a diamond quantum memory, *PRX Quantum* **5**, 010303 (2024).
- [26] C. Knaut, A. Suleymanzade, Y.-C. Wei, D. Assumpcao, P.-J. Stas, Y. Huan, B. Machielse, E. Knall, M. Sutula, G. Baranes, *et al.*, Entanglement of nanophotonic quantum memory nodes in a telecom network, *Nature* **629**, 573 (2024).
- [27] P. Kumar, Quantum frequency conversion, *Optics letters* **15**, 1476 (1990).

[28] J. Huang and P. Kumar, Observation of quantum frequency conversion, *Physical review letters* **68**, 2153 (1992).

[29] J. S. Pelc, C. Langrock, Q. Zhang, and M. M. Fejer, Influence of domain disorder on parametric noise in quasi-phase-matched quantum frequency converters, *Optics letters* **35**, 2804 (2010).

[30] H. J. McGuinness, M. G. Raymer, C. J. McKinstry, and S. Radic, Quantum frequency translation of single-photon states in a photonic crystal fiber, *Physical review letters* **105**, 093604 (2010).

[31] J. S. Pelc, L. Ma, C. Phillips, Q. Zhang, C. Langrock, O. Slattery, X. Tang, and M. M. Fejer, Long-wavelength-pumped upconversion single-photon detector at 1550 nm: performance and noise analysis, *Optics express* **19**, 21445 (2011).

[32] K. De Greve, L. Yu, P. L. McMahon, J. S. Pelc, C. M. Natarajan, N. Y. Kim, E. Abe, S. Maier, C. Schneider, M. Kamp, *et al.*, Quantum-dot spin-photon entanglement via frequency downconversion to telecom wavelength, *Nature* **491**, 421 (2012).

[33] P. S. Kuo, J. S. Pelc, O. Slattery, Y.-S. Kim, M. M. Fejer, and X. Tang, Reducing noise in single-photon-level frequency conversion, *Optics letters* **38**, 1310 (2013).

[34] B. Albrecht, P. Farrera, X. Fernandez-Gonzalvo, M. Cristiani, and H. De Riedmatten, A waveguide frequency converter connecting rubidium-based quantum memories to the telecom c-band, *Nature communications* **5**, 3376 (2014).

[35] Q. Li, M. Davanço, and K. Srinivasan, Efficient and low-noise single-photon-level frequency conversion interfaces using silicon nanophotonics, *Nature Photonics* **10**, 406 (2016).

[36] T. Walker, K. Miyanishi, R. Ikuta, H. Takahashi, S. Vartabi Kashanian, Y. Tsujimoto, K. Hayasaka, T. Yamamoto, N. Imoto, and M. Keller, Long-distance single photon transmission from a trapped ion via quantum frequency conversion, *Physical review letters* **120**, 203601 (2018).

[37] R. Ikuta, T. Kobayashi, T. Kawakami, S. Miki, M. Yabuno, T. Yamashita, H. Terai, M. Koashi, T. Mukai, T. Yamamoto, *et al.*, Polarization insensitive frequency conversion for an atom-photon entanglement distribution via a telecom network, *Nature communications* **9**, 1997 (2018).

[38] V. Esfandyarpour, C. Langrock, and M. Fejer, Cascaded downconversion interface to convert single-photon-level signals at 650 nm to the telecom band, *Optics Letters* **43**, 5655 (2018).

[39] N. Maring, D. Lago-Rivera, A. Lenhard, G. Heinze, and H. de Riedmatten, Quantum frequency conversion of memory-compatible single photons from 606 nm to the telecom c-band, *Optica* **5**, 507 (2018).

[40] J. D. Siverns, J. Hannegan, and Q. Quraishi, Neutral-atom wavelength-compatible 780 nm single photons from a trapped ion via quantum frequency conversion, *Physical Review Applied* **11**, 014044 (2019).

[41] A. Singh, Q. Li, S. Liu, Y. Yu, X. Lu, C. Schneider, S. Höfling, J. Lawall, V. Verma, R. Mirin, *et al.*, Quantum frequency conversion of a quantum dot single-photon source on a nanophotonic chip, *Optica* **6**, 563 (2019).

[42] X. Lu, G. Moille, A. Rao, and K. Srinivasan, Proposal for noise-free visible-telecom quantum frequency conversion through third-order sum and difference frequency generation, *Optics letters* **46**, 222 (2021).

[43] T. van Leent, M. Bock, F. Fertig, R. Garthoff, S. Eppelt, Y. Zhou, P. Malik, M. Seubert, T. Bauer, W. Rosenfeld, *et al.*, Entangling single atoms over 33 km telecom fibre, *Nature* **607**, 69 (2022).

[44] X. Wang, X. Jiao, B. Wang, Y. Liu, X.-P. Xie, M.-Y. Zheng, Q. Zhang, and J.-W. Pan, Quantum frequency conversion and single-photon detection with lithium niobate nanophotonic chips, *npj Quantum Information* **9**, 38 (2023).

[45] Z.-Q.-Z. Han, Z.-Y. Zhou, and B.-S. Shi, Quantum frequency transducer and its applications, *Advanced Devices & Instrumentation* **4**, 0030 (2023).

[46] D. Kielpinski, J. F. Corney, and H. M. Wiseman, Quantum optical waveform conversion, *Physical Review Letters* **106**, 130501 (2011).

[47] M. Karpiński, M. Jachura, L. J. Wright, and B. J. Smith, Bandwidth manipulation of quantum light by an electro-optic time lens, *Nature Photonics* **11**, 53 (2017).

[48] M. Petruzzella, T. Xia, F. Pagliano, S. Birindelli, L. Midolo, Z. Zobenica, L. Li, E. Linfield, and A. Fiore, Fully tuneable, purcell-enhanced solid-state quantum emitters, *Applied Physics Letters* **107** (2015).

[49] H. Kaupp, T. Hümmer, M. Mader, B. Schleuderer, J. Benedikter, P. Haeusser, H.-C. Chang, H. Fedder, T. W. Hänsch, and D. Hunger, Purcell-enhanced single-photon emission from nitrogen-vacancy centers coupled to a tunable microcavity, *Physical Review Applied* **6**, 054010 (2016).

[50] K. Wintersperger, F. Dommert, T. Ehmer, A. Hoursanov, J. Klepsch, W. Mauerer, G. Reuber, T. Strohm, M. Yin, and S. Luber, Neutral atom quantum computing hardware: performance and end-user perspective, *EPJ Quantum Technology* **10**, 32 (2023).

[51] S. A. Moses, C. H. Baldwin, M. S. Allman, R. Ancona, L. Ascarrunz, C. Barnes, J. Bartolotta, B. Bjork, P. Blanchard, M. Bohn, *et al.*, A race-track trapped-ion quantum processor, *Physical Review X* **13**, 041052 (2023).

[52] M. Kjaergaard, M. E. Schwartz, J. Braumüller, P. Krantz, J. I.-J. Wang, S. Gustavsson, and W. D. Oliver, Superconducting qubits: Current state of play, *Annual Review of Condensed Matter Physics* **11**, 369 (2020).

[53] A. Ruskuc, C.-J. Wu, E. Green, S. Hermans, W. Pajak, J. Choi, and A. Faraon, Multiplexed entanglement of multi-emitter quantum network nodes, *Nature* , 1 (2025).

[54] D. Zhu, L. Shao, M. Yu, R. Cheng, B. Desiatov, C. Xin, Y. Hu, J. Holzgrafe, S. Ghosh, A. Shams-Ansari, *et al.*, Integrated photonics on thin-film lithium niobate, *Advances in Optics and Photonics* **13**, 242 (2021).

[55] X. Chen, J. Lin, and K. Wang, A review of silicon-based integrated optical switches, *Laser & Photonics Reviews* **17**, 2200571 (2023).

[56] C. Young, A. Safari, P. Huft, J. Zhang, E. Oh, R. Chinnarasu, and M. Saffman, An architecture for quantum networking of neutral atom processors, *Applied Physics B* **128**, 151 (2022).

[57] J. Wurtz, A. Bylinskii, B. Braverman, J. Amato-Grill, S. H. Cantu, F. Huber, A. Lukin, F. Liu, P. Weinberg, J. Long, *et al.*, Aquila: Quera's 256-qubit neutral-atom quantum computer, *arXiv preprint arXiv:2306.11727* (2023).

[58] T. N. Bandi, A comprehensive overview of atomic clocks and their applications, *Demo Journal* **1**, 40 (2024).

[59] C. Derntl, M. Schneider, J. Schalko, A. Bittner, J. Schmiedmayer, U. Schmid, and M. Trupke, Arrays of open, independently tunable microcavities, *Optics express* **22**, 22111 (2014).

[60] J. Gallego, S. Ghosh, S. K. Alavi, W. Alt, M. Martinez-Dorantes, D. Meschede, and L. Ratschbacher, High-finesse fiber fabry–perot cavities: stabilization and mode matching analysis, *Applied Physics B* **122**, 1 (2016).

[61] G. Wachter, S. Kuhn, S. Minniberger, C. Salter, P. Asenbaum, J. Millen, M. Schneider, J. Schalko, U. Schmid, A. Felgner, *et al.*, Silicon microcavity arrays with open access and a

finesse of half a million, *light: science & applications* **8**, 37 (2019).

[62] N. Jin, C. A. McLemore, D. Mason, J. P. Hendrie, Y. Luo, M. L. Kelleher, P. Kharel, F. Quinlan, S. A. Diddams, and P. T. Rakich, Micro-fabricated mirrors with finesse exceeding one million, *Optica* **9**, 965 (2022).

[63] T. H. Doherty, A. Kuhn, and E. Kassa, Multi-resonant open-access microcavity arrays for light matter interaction, *Optics Express* **31**, 6342 (2023).

[64] B. Grinkemeyer, E. Guardado-Sanchez, I. Dimitrova, D. Shchepanovich, G. E. Mandopoulou, J. Borregaard, V. Vuletić, and M. D. Lukin, Error-detected quantum operations with neutral atoms mediated by an optical cavity, *Science* **387**, 1301 (2025).

[65] W. Huie, S. G. Menon, H. Bernien, and J. P. Covey, Multiplexed telecommunication-band quantum networking with atom arrays in optical cavities, *Physical Review Research* **3**, 043154 (2021).

[66] J. Ramette, J. Sinclair, Z. Vendeiro, A. Rudelis, M. Cetina, and V. Vuletić, Any-to-any connected cavity-mediated architecture for quantum computing with trapped ions or rydberg arrays, *PRX Quantum* **3**, 010344 (2022).

[67] N. I. Zheludev and E. Plum, Reconfigurable nanomechanical photonic metamaterials, *Nature nanotechnology* **11**, 16 (2016).

[68] M. Wuttig, H. Bhaskaran, and T. Taubner, Phase-change materials for non-volatile photonic applications, *Nature photonics* **11**, 465 (2017).

[69] D. Marpaung, J. Yao, and J. Capmany, Integrated microwave photonics, *Nature photonics* **13**, 80 (2019).

[70] W. Zhang, R. Mazzarello, M. Wuttig, and E. Ma, Designing crystallization in phase-change materials for universal memory and neuro-inspired computing, *Nature Reviews Materials* **4**, 150 (2019).

[71] D. Pérez, I. Gasulla, P. Das Mahapatra, and J. Capmany, Principles, fundamentals, and applications of programmable integrated photonics, *Advances in Optics and Photonics* **12**, 709 (2020).

[72] Z. Fang, J. Zheng, A. Saxena, J. Whitehead, Y. Chen, and A. Majumdar, Non-volatile reconfigurable integrated photonics enabled by broadband low-loss phase change material, *Advanced Optical Materials* **9**, 2002049 (2021).

[73] C. Wu, H. Yu, S. Lee, R. Peng, I. Takeuchi, and M. Li, Programmable phase-change meta-

surfaces on waveguides for multimode photonic convolutional neural network, *Nature communications* **12**, 96 (2021).

[74] J. H. Ko, Y. J. Yoo, Y. Lee, H.-H. Jeong, and Y. M. Song, A review of tunable photonics: Optically active materials and applications from visible to terahertz, *IScience* **25** (2022).

[75] X. Xue, Y. Xuan, C. Wang, P.-H. Wang, Y. Liu, B. Niu, D. E. Leaird, M. Qi, and A. M. Weiner, Thermal tuning of kerr frequency combs in silicon nitride microring resonators, *Optics express* **24**, 687 (2016).

[76] M. Rahmani, L. Xu, A. E. Miroshnichenko, A. Komar, R. Camacho-Morales, H. Chen, Y. Zárate, S. Kruk, G. Zhang, D. N. Neshev, *et al.*, Reversible thermal tuning of all-dielectric metasurfaces, *Advanced Functional Materials* **27**, 1700580 (2017).

[77] K.-H. Luo, S. Brauner, C. Eigner, P. R. Sharapova, R. Ricken, T. Meier, H. Herrmann, and C. Silberhorn, Nonlinear integrated quantum electro-optic circuits, *Science advances* **5**, eaat1451 (2019).

[78] M. Asobe, D. Yagi, Y. Kawabata, T. Umeki, K. Enbutsu, T. Kazama, and R. Kasahara, Broadband optical parametric amplification using ppls waveguide pumped by detuned second harmonic, *Optics Express* **30**, 9473 (2022).

[79] L. Kang, Y. Cui, S. Lan, S. P. Rodrigues, M. L. Brongersma, and W. Cai, Electrifying photonic metamaterials for tunable nonlinear optics, *Nature communications* **5**, 4680 (2014).

[80] S. Abel, T. Stöferle, C. Marchiori, D. Caimi, L. Czornomaz, M. Stuckelberger, M. Sousa, B. J. Offrein, and J. Fompeyrine, A hybrid barium titanate–silicon photonics platform for ultraefficient electro-optic tuning, *Journal of Lightwave Technology* **34**, 1688 (2016).

[81] G. Sinatkas, T. Christopoulos, O. Tsilipakos, and E. E. Kriezis, Electro-optic modulation in integrated photonics, *Journal of Applied Physics* **130** (2021).

[82] C. W. Wong, P. T. Rakich, S. G. Johnson, M. Qi, H. I. Smith, E. P. Ippen, L. C. Kimerling, Y. Jeon, G. Barbastathis, and S.-G. Kim, Strain-tunable silicon photonic band gap microcavities in optical waveguides, *Applied physics letters* **84**, 1242 (2004).

[83] L. A. Fernandes, J. R. Grenier, P. R. Herman, J. S. Aitchison, and P. V. Marques, Stress induced birefringence tuning in femtosecond laser fabricated waveguides in fused silica, *Optics express* **20**, 24103 (2012).

[84] M. Zapf, R. R"oder, K. Winkler, L. Kaden, J. Greil, M. Wille, M. Grundmann, R. Schmidt-Grund, A. Lugstein, and C. Ronning, Dynamical tuning of nanowire lasing spectra, *Nano*

letters **17**, 6637 (2017).

[85] R. Tyumenev, J. Hammer, N. Joly, P. S. J. Russell, and D. Novoa, Tunable and state-preserving frequency conversion of single photons in hydrogen, *Science* **376**, 621 (2022).

[86] R. Yanagimoto, B. A. Ash, M. M. Sohoni, M. M. Stein, Y. Zhao, F. Presutti, M. Jankowski, L. G. Wright, T. Onodera, and P. L. McMahon, Programmable on-chip nonlinear photonics, arXiv preprint arXiv:2503.19861 (2025).

[87] A. Malik, C. Xiang, L. Chang, W. Jin, J. Guo, M. Tran, and J. Bowers, Low noise, tunable silicon photonic lasers, *Applied Physics Reviews* **8** (2021).

[88] X. Lu, L. Chang, M. A. Tran, T. Komljenovic, J. E. Bowers, and K. Srinivasan, Emerging integrated laser technologies in the visible and short near-infrared regimes, *Nature Photonics* , 1 (2024).

[89] E. Kaur, H. Shapourian, J. Zhao, M. Kilzer, R. Kompella, and R. Nejabati, Optimized quantum circuit partitioning across multiple quantum processors, arXiv preprint arXiv:2501.14947 (2025).

[90] H. Zhang, Y. Xu, H. Hu, K. Yin, H. Shapourian, J. Zhao, R. R. Kompella, R. Nejabati, and Y. Ding, Optimizing quantum communication for quantum data centers with reconfigurable networks, arXiv preprint arXiv:2412.04837 (2024).

[91] M. Stepanovsky, A comparative review of mems-based optical cross-connects for all-optical networks from the past to the present day, *IEEE Communications Surveys & Tutorials* **21**, 2928 (2019).

[92] W. Shi, H. Yun, C. Lin, M. Greenberg, X. Wang, Y. Wang, S. T. Fard, J. Flueckiger, N. A. Jaeger, and L. Chrostowski, Ultra-compact, flat-top demultiplexer using anti-reflection contra-directional couplers for cwdm networks on silicon, *Optics express* **21**, 6733 (2013).

[93] HUBER+SUHNER, Polatis quantum switch (2024), accessed: 2025-02-05.

[94] A. Michaels and E. Yablonovitch, Inverse design of near unity efficiency perfectly vertical grating couplers, *Optics express* **26**, 4766 (2018).

[95] D. H. Jundt, Temperature-dependent sellmeier equation for the index of refraction, n e, in congruent lithium niobate, *Optics letters* **22**, 1553 (1997).

[96] B.-S. Song, T. Asano, S. Jeon, H. Kim, C. Chen, D. D. Kang, and S. Noda, Ultrahigh-Q photonic crystal nanocavities based on 4H silicon carbide, *Optica* **6**, 991 (2019).

[97] D. M. Lukin, C. Dory, M. A. Gaidry, K. Y. Yang, S. D. Mishra, R. Trivedi, M. Radu-

laski, S. Sun, D. Vercruyse, G. H. Ahn, and J. Vuckovic, 4H-silicon-carbide-on-insulator for integrated quantum and nonlinear photonics, *Nature Photonics* **14**, 330 (2020).

[98] F. Samara, A. Martin, C. Autebert, M. Karpov, T. J. Kippenberg, H. Zbinden, and R. Thew, High-rate photon pairs and sequential time-bin entanglement with Si_3N_4 microring resonators, *Opt. Express* **27**, 19309 (2019).

[99] G. Moille, D. Westly, E. F. Perez, M. Metzler, G. Simelgor, and K. Srinivasan, Integrated buried heaters for efficient spectral control of air-clad microresonator frequency combs, *APL Photonics* **7**, 126104 (2022).

[100] N. B. Lingaraju, H.-H. Lu, S. Seshadri, D. E. Leaird, A. M. Weiner, and J. M. Lukens, Adaptive bandwidth management for entanglement distribution in quantum networks, *Optica* **8**, 329 (2021).

[101] F. Appas, F. Baboux, M. I. Amanti, A. Lemaître, F. Boitier, E. Diamanti, and S. Ducci, Flexible entanglement-distribution network with an algaas chip for secure communications, *npj Quantum Information* **7**, 118 (2021).

[102] M. Alshowkan, B. P. Williams, P. G. Evans, N. S. Rao, E. M. Simmerman, H.-H. Lu, N. B. Lingaraju, A. M. Weiner, C. E. Marvinney, Y.-Y. Pai, *et al.*, Reconfigurable quantum local area network over deployed fiber, *PRX Quantum* **2**, 040304 (2021).

[103] M. Alshowkan, P. G. Evans, B. P. Williams, N. S. Rao, C. E. Marvinney, Y.-Y. Pai, B. J. Lawrie, N. A. Peters, and J. M. Lukens, Advanced architectures for high-performance quantum networking, *Journal of Optical Communications and Networking* **14**, 493 (2022).

[104] M. Alshowkan, J. M. Lukens, H.-H. Lu, B. T. Kirby, B. P. Williams, W. P. Grice, and N. A. Peters, Broadband polarization-entangled source for c+ l-band flex-grid quantum networks, *Optics Letters* **47**, 6480 (2022).

[105] H.-H. Lu, M. Alshowkan, J. Alnas, J. M. Lukens, and N. A. Peters, Procrustean entanglement concentration in quantum-classical networking, *Physical Review Applied* **21**, 044027 (2024).

[106] A. Miloshevsky, L. M. Cohen, K. V. Myilswamy, M. Alshowkan, S. Fatema, H.-H. Lu, A. M. Weiner, and J. M. Lukens, Cmos photonic integrated source of ultrabroadband polarization-entangled photons, *arXiv preprint arXiv:2402.09307* (2024).

[107] L. Li, L. D. Santis, I. B. Harris, K. C. Chen, Y. Gao, I. Christen, H. Choi, M. Trusheim, Y. Song, C. Errando-Herranz, *et al.*, Heterogeneous integration of spin–photon interfaces with a cmos platform, *Nature* , 1 (2024).

[108] T. Utsugi, A. Goban, Y. Tokunaga, H. Goto, and T. Aoki, Gaussian-wave-packet model for single-photon generation based on cavity quantum electrodynamics under adiabatic and nonadiabatic conditions, *Physical Review A* **106**, 023712 (2022).

[109] DiCon Fiberoptics, Scd-0474e (generic, sx2 model, single mode fiber, performance grade) (2025), accessed: 2025-02-05.

[110] D. T. Neilson, R. Frahm, P. Kolodner, C. Bolle, R. Ryf, J. Kim, A. Papazian, C. Nuzman, A. Gasparyan, N. Basavanhally, *et al.*, 256× 256 port optical cross-connect subsystem, *Journal of Lightwave Technology* **22**, 1499 (2004).

[111] H. Aghaee Rad, T. Ainsworth, R. Alexander, B. Altieri, M. Askarani, R. Baby, L. Banchi, B. Baragiola, J. Bourassa, R. Chadwick, *et al.*, Scaling and networking a modular photonic quantum computer, *Nature* , 1 (2025).

[112] S. Hooten, T. V. Vaerenbergh, P. Sun, S. Mathai, Z. Huang, and R. G. Beausoleil, Adjoint optimization of efficient cmos-compatible si-sin vertical grating couplers for dwdm applications, *Journal of Lightwave Technology* **38**, 3422 (2020).

[113] I. Esmaeil Zadeh, J. Chang, J. W. Los, S. Gyger, A. W. Elshaari, S. Steinhauer, S. N. Dorenbos, and V. Zwiller, Superconducting nanowire single-photon detectors: A perspective on evolution, state-of-the-art, future developments, and applications, *Applied Physics Letters* **118** (2021).

[114] M. W. Puckett and N. A. Krueger, Broadband, ultrahigh efficiency fiber-to-chip coupling via multilayer nanophotonics, *Applied Optics* **60**, 4340 (2021).

[115] K. Alexander, A. Bahgat, A. Benyamin, D. Black, D. Bonneau, S. Burgos, B. Burridge, G. Campbell, G. Catalano, A. Ceballos, *et al.*, A manufacturable platform for photonic quantum computing, *arXiv preprint arXiv:2404.17570* (2024).

[116] R. Loudon, The raman effect in crystals, *Advances in Physics* **13**, 423 (1964).

[117] I. Kaminow and W. Johnston Jr, Quantitative determination of sources of the electro-optic effect in linb o 3 and lita o 3, *Physical Review* **160**, 519 (1967).

[118] M. Bache and R. Schiek, Review of measurements of kerr nonlinearities in lithium niobate: the role of the delayed raman response, *arXiv preprint arXiv:1211.1721* (2012).

[119] R. W. Boyd, *Nonlinear Optics*, 4th ed. (Elsevier, Oxford, 2020).

[120] J. S. Pelc, *Frequency conversion of single photons: physics, devices, and applications* (Stanford University, 2012).

- [121] W. Johnston Jr and I. Kaminow, Temperature dependence of raman and rayleigh scattering in linbo₃ and lita₃, *Physical Review* **168**, 1045 (1968).
- [122] N. Kokanyan, D. Chapron, and M. D. Fontana, Temperature dependence of raman scattering and anharmonic properties in linbo₃, *Applied Physics A* **117**, 1147 (2014).